NRC Publications Archive
Archives des publications du CNRC

Fluid Flow Modeling in a 55%Al-Zn Coating Metal Pot

Willis, David J.; Ilinca, Florin; Ajersch, Frank; Setargew, Nega

Questions? Contact the NRC Publications Archive team at
PublicationsArchive-ArchivesPublications@nrc-cnrc.gc.ca. If you wish to email the authors directly, please see the
first page of the publication for their contact information.

Vous avez des questions? Nous pouvons vous aider. Pour communiquer directement avec un auteur, consultez la
première page de la revue dans laquelle son article a été publié afin de trouver ses coordonnées. Si vous n'arrivez
pas à les repérer, communiquez avec nous à PublicationsArchive-ArchivesPublications@nrc-cnrc.gc.ca.

Conseil national de recherches
Canada

National Research Council
Canada

Institut des matériaux industriels

Industrial Materials Institute

Fiche d'information et d'autorisation
pour documents internes, externes et conférences

Année calendrier
2005

No de projet   14J

Titre du document

Fluid flow modeling in a 55%Al-Zn coating metal pot

Statut du document   Général

Types de document

☐ Sommaire (Abstract)   Écrit final suivra ? ☐ Non ☐ Si Oui Date _____

☒ Document soumis pour publication

Si un sommaire (abstract) a été soumis précédemment,
veuillez indiquer les numéros   IMI _____   CNRC _____

À présenter
dans le cadre de   CFD2005; Fourth International Conference on CFD in the Oil and Gas, Metallurgical &
                          Process Industries

Date de la conférence 6-8 Juin, 2005   Lieu Trondheim, Norway

À paraître dans _____   Date _____

☐ Rapport

   ☐ Technique   ☐ Industriel de servic

☐ Autre (spécifiez) _____

À être complétée par votre secrétaire. Veuillez l'aviser lorsque l'information sera disponible.

☐ Publication   Année calendrier
                       2005

   ☐ Revues et livres avec comité de lecture

   ☐ Procès-verbaux de conférence avec comité de lecture

   ☐ Procès-verbaux de conférence sans comité de lecture

Si un sommaire (abstract) a été soumis précédemment,
veuillez indiquer les numéros   IMI _____   CNRC CNRC _____

   Paru dans (vol. pp)

Partenaires BlueScope Steel, École Polytechnique de Montréal

Déclaration d'invention _____   Date _____

Demande de brevet déposée _____   Pays _____

Si non, explications: _____

| Auteur (nom prénom) | Affiliation | | | Signature | Date |
	Section	Groupe	Externe BlueScope		
Willie D.				Dan Wills	21/3/05
Ilinca F.	504000	504100		Frank Ilinca	23/2/2005
Ajersch F.			Polytechnique		23/2/2005
Sétargew N.			BlueScope	Ned Setargew	24/3/2005

Je certifie, en tant que premier auteur, que j'ai vérifié avec le(s) partenaire(s) qu'il(s) n'a (n'ont) pas d'objection à ce document.

Approbations: _____   B. Ch _____   29-05-05

Signature   Date   Signature   Date   Signature   Date
Chef de groupe   Directeur de section   Directeur général

Numéro IMI 2005 109087 g   CNRC 47904

FLUID FLOW MODELING IN A 55%Al-Zn COATING METAL POT

David J. WILLIS[1], Florin ILINCA[2], Frank AJERSCH[3] and Nega SETARGEW[1]

[1] BlueScope Steel Research Laboratory, Port Kembla, Australia

[2] Industrial Materials Institute, National Research Council, Québec, Canada

[3] École Polytechnique de Montréal, Montréal, Canada

ABSTRACT

Numerical simulations were carried out to model the fluid flow and temperature distribution in two channel inductor pots used for the manufacture of 55%Al-Zn coated steel. The software used for this work was developed by the Industrial Materials Institute of the National Research Council of Canada (IMI-NRC) and includes k-ε turbulence modeling for fluid flow and heat transfer adapted for the simulation of a sequence of operating parameters. The simulations included particle tracking in the molten bath of 55%Al-Zn alloy. The model includes a full-scale model of the pot geometry, immersed hardware and the traversing steel strip. Fluid flow arising from the moving strip in the bath was also modelled. BlueScope Steel experiences bottom dross formation at three of its eight ZINCALUME lines. Numerical solutions are presented for two pots: MCL4 at Western Port that has excessive bottom dross build-up and MCL1 at Port Kembla that does not. The paper will describe some of the results of the modeling work, highlighting the differences in fluid flow and temperature distribution in the two pots that are likely to contribute to different propensities to bottom dross formation. The objective of this work is to analyze this problem using Computational Fluid Dynamics (CFD) modeling.

NOMENCLATURE

c_p specific heat
g   gravity
k turbulence kinetic energy (TKE)
p pressure
t time
T temperature
u   velocity
β thermal expansion coefficient
λ thermal conductivity
ε TKE dissipation
ρ density
μ dynamic viscosity

INTRODUCTION

BlueScope Steel's Experience

In 2000, three of BlueScope Steel's eight ZINCALUME coating pots had problems with excessive bottom dross formation: MCL4 at Western Port, BlueScope Steel Indonesia and BlueScope Steel Thailand (BlueScope Steel was formerly known as BHP Steel). The first two continue to experience excessive bottom dross formation. A concerted problem solving effort began in early 2001 in order to identify why some ZINCALUME coating pots are more prone to bottom dross formation than others and several hypotheses were put forward (Willis and Setargew, 2002). Work has continued to test these hypotheses and to develop strategies to overcome excessive bottom dross and the associated problems of rapid sink-roll build-up and coating defects. Bottom dross has been shown to be a mixture of intermetallic particles and entrained bath metal. The intermetallic particles originate when the iron, dissolved in the 55%Al-Zn melt, exceeds the solubility limit. Small precipitates of the intermetallic compound are known to be suspended in the melt (Willis and Setargew, 2002; Setargew and Willis, 2003) and one hypothesis for the different propensity for bottom dross formation in some pots is that the flow conditions in some pots create a greater tendency for the particles to settle to the bottom of the pot. Another hypothesis is that temperature fluctuations in the pot promote precipitation and increased settling of the particles. To help test these hypotheses, a fluid flow model was developed. The model calculates the fluid flow and the temperature distribution in the pot. The CFD modeling was carried out by the National Research Council Canada (NRC) at the Industrial Materials Institute (IMI) in Boucherville, Québec. The initial objective was to compare the fluid flow in a pot with bottom dross problems (MCL4) to one without bottom dross problems (MCL1). Results from this study were presented at the Galvatech 2004 Conference (Willis, Ilinca and Ajersch, 2004). The first reported results were obtained by using the side inductors of the MCL1 pot inadvertently located closer to the exit end of pot than in the actual configuration. Computations using the correct position of the side inductors were carried out and indicate that the conclusions of the previous study were correct. In this paper we present the results for the corrected pot configuration as well as a study of the movement of dross particles in the MCL1 and MCL4 pots.

CFD Modeling of Galvanizing Pots

The first attempts to model galvanizing pots were reported by Gagné, Paré and Ajersch, 1992. Water modeling was used to validate the modeling approach and there were attempts to measure the fluid flow in a galvanizing bath by two methods (Toussaint et al, 1996; Gagné and Ajersch, 1995). The numerical modeling of galvanizing pots has been further developed over the past 10 years (Paré and Ajersch, 1995; Gagné and Gang, 1998; Otsuka et al, 1998; Evans and Treadgold, 1999). Since 1998 CFD modeling of galvanizing pots has been sponsored by ILZRO as research project ZCO-8, "Computer aids for galvanizing bath management". The project was

undertaken by École Polytechnique de Montréal and numerical modeling was done by IMI-NRC. For instance, the important influence of thermal buoyancy effects has been demonstrated and the effect of various process parameters was studied (Ajersch et al, 2001).

There has been no published work on the modeling of 55% Al-Zn pots with channel inductors although coreless pots for 55%Al-Zn coated steel production have been modeled (Kobayashi et al, 1996). Most galvanizing pots differ from 55%Al-Zn pots in several essential features. Galvanizing pots are often of greater volume and contain a much greater mass of molten metal due to the higher density of zinc. They operate at lower temperatures 460 vs 600°C, and usually use only two inductors located at each side of the pot that are often offset toward the rear of the pot in order to promote melting of the zinc ingots when no premelt pot is used. For galvanizing operations the temperature of the strip entering the melt is often similar to the bath temperature (strip and bath are approximately at 450-460°C). For 55%Al-Zn operations the strip entry temperature is typically between 520-580°C with a pot temperature of 590-610°C. Therefore, the temperature difference between the melt and the strip is more significant than for a galvanizing pot. In most operations each pot has four inductors, one at each side, one at the front and one at the back of the pot. Finally, the material properties are also different (Table 1). For instance, the viscosity of zinc is about 2.5 times higher than that of 55%Al-Zn. For all these reasons, the fluid flow and temperature distribution in a 55%Al-Zn pot are expected to differ from those in a galvanizing pot. The nature of the CFD model will be first described, and an attempt has been made to validate the model by comparing temperature measurements in the pot with results of the model. Selected results from the model are then presented in order to identify differences between the fluid flow and temperature distribution in MCL4 and MCL1.

Property	55%Al-Zn at 600°C	Zn-0.14%Al at 460°C
Density (kg/m³)	3327	6600
Viscosity (Pa·s)	0.001648	0.004
Specific heat (J/kg·K)	860	512
Thermal conductivity (W/m·K)	50	60
Thermal expansion coefficient (K⁻¹)	1.153×10^{-4}	1.666×10^{-4}

Table 1: Material properties of 55%Al-Zn and Zn-0.14%Al used by NRC-IMI in CFD modeling.

NUMERICAL MODEL

Model input

Detailed dimensions of the metal coating pot and the immersed pot hardware were obtained from engineering drawings. The significant differences between MCL1 and MCL4 (see Figure 1) are:
1. MCL4 is a much larger pot with a volume of 24.7 m³ compared to MCL1's 13.9 m³.
2. MCL4 is rectangular in shape and MCL1 is square.
3. MCL4 has a curved hearth with the axis of curvature parallel to the sink-roll axis. MCL1 has a flat bottomed hearth (it does have sloping sections of the pot walls but these are on the operator and drive side walls).

4. MCL4 has its sink-roll, and stabilizer roll, located deeper in the pot.
5. MCL4 has inductor throat outlets located higher up the walls of the pot compared to MCL1.
6. MCL4 side wall inductors are located in the centre of the side walls whereas MCL1 has the inductors located closer to the exit end of the pot.
7. MCL4 has a different design of the end of the sink-roll, having fillets.
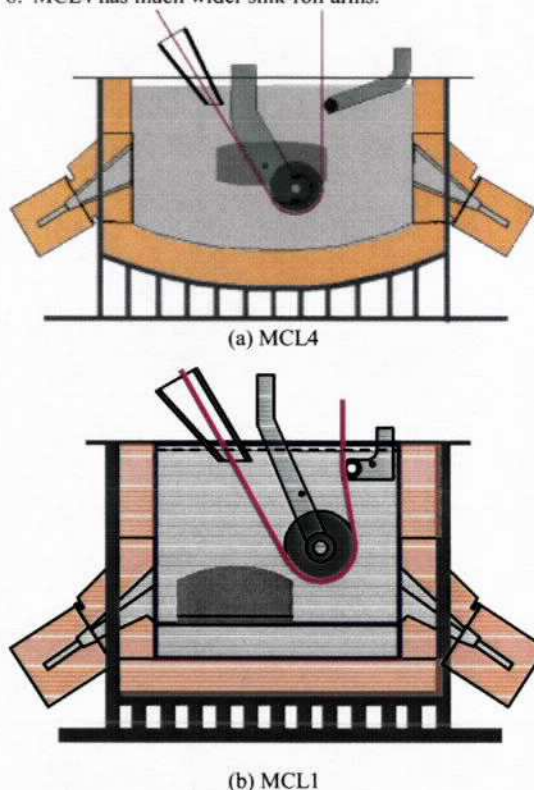8. MCL4 has much wider sink-roll arms.

(a) MCL4

(b) MCL1

Figure 1: Schematic of the MCL4 and MCL1 pots

The numerical simulation was carried out for line operating conditions corresponding to running a recrystallised grade 0.55 mm x 1200 mm ZINCALUME G300 AZ150. The following parameters were specified for each case: line speed, strip entry temperature, pot temperature, and inductor power and firing sequence. The inductors in MCL1 and MCL4 operate at one of three transformer tap settings. Pot temperature control is achieved by switching the inductors periodically between these settings with a period of 5 to 15 minutes or longer. The tap settings are different for the two pots (Table 2). For the cases considered neither MCL1 or MCL4 did not make use of the high power setting.

Pot	Low	Intermediate	High
MCL1	48	139	339*
MCL4	31	235	300

* Entry and exit 353kW; operator and drive 325kW

Table 2: Inductor Power Settings for ZINCALUME Pots (kW).

The flow from the inductors was modeled using information provided by AJAX, the inductor supplier. At a

given power setting the inductors impose a certain mass flow rate and temperature rise on the molten metal passing through them. The MCL1 pot was fitted with jet flow inductors while the MCL4 pot had the older style square channeled GU2 (hereafter known as conventional inductors). For the same power setting, jet flow inductors give a higher mass flow rate and a proportionately lower temperature rise (see Table 3).

Coating Pot	MCL1		MCL4	
Line speed	95 m/min		130 m/min	
Pot temperature[a]	600°C (593°C)		608°C	
Strip entry temp.[a]	515°C (535.7°C)		550°C (556°C)	
Case	1C	1D	4B	4C
Ind. Power Setting	High	Interm.	Interm.	Low
Specified power, kW (Power used in the model)[b]	339kW (366.4)	139kW (143.3)	235kW (227.5)	31 kW (36.4)
Time at inductor setting (min)	2.2	10	14	4
Output metal flow rate (t/h)[c]	125	79	45.4	21.8
Output metal temp. increase	12.2°C	7.6°C	21°C	7°C

(a) The model uses the values in brackets based on heat balance calculations, see (Willis & Setargew, 2002) for details.
(b) The specified power is as indicated by AJAX. The power calculated from the specified flow rate and temperature increase is indicated in brackets and was used in the model.
(c) Information provided by AJAX, t/h is metric tonnes/h

Table 3: Line and pot parameters.

Physical properties of the liquid 55%Al-Zn alloy are indicated in Table 1. All simulations were computed using the IMI fluid dynamic solver. The computational domain was discretized using 4-node tetrahedral finite elements. For MCL4 the mesh has 82,590 nodes and 452,887 elements and for MCL1 the corresponding figures were 63,823 and 320,624.

Numerical model

The numerical model assumes that the melt behaves as a Newtonian fluid and that the flow is turbulent. Buoyancy effects are considered using the Boussinesq approximation. It was assumed that the flow is symmetrical with respect to the pot mid plane and consequently only one half of the pot was modeled. Time dependent effects are included and solutions were obtained at different time intervals. The flow inside the bath is therefore described by the incompressible Navier-Stokes equations:

$$\rho_0(D\mathbf{u}/Dt) = -\nabla p + \nabla \cdot [2(\mu + \mu_T)\dot{\gamma}(\mathbf{u})] - \rho_0 \mathbf{g}\beta(T - T_0) \quad (1)$$

$$\nabla \cdot \mathbf{u} = 0 \quad (2)$$

where $D/Dt = \partial/\partial t + \mathbf{u} \cdot \nabla$ is the particular derivative, $\dot{\gamma}(\mathbf{u}) = (\nabla \mathbf{u} + \nabla \mathbf{u}^T)/2$ is the strain rate tensor, ρ_0 is the density at the reference temperature T_0, μ is the fluid viscosity, μ_T is the turbulent viscosity, g is the gravity and β is the thermal expansion coefficient. Temperature T is obtained by solving the energy equation:

$$\rho c_p (DT/Dt) = \nabla \cdot [(\lambda + \lambda_T)\nabla T] \quad (3)$$

where c_p is the specific heat, λ is the thermal conductivity, and λ_T is the turbulent thermal conductivity given by

$$\lambda_T = \mu_T c_p / \mathrm{Pr}_T \quad (4)$$

with the turbulent Prandtl number Pr_T considered equal to unity. The turbulent viscosity μ_T is computed using the standard $k - \varepsilon$ model of turbulence (Launder and Spalding, 1972):

$$\mu_T = \rho C_\mu k^2 / \varepsilon \quad (5)$$

The turbulence kinetic energy k and its dissipation rate ε are obtained from the transport equations:

$$\rho(Dk/Dt) = \nabla \cdot [(\mu + \mu_T / \sigma_k)\nabla k] + P + G - \rho \varepsilon \quad (6)$$

$$\rho(D\varepsilon/Dt) = \nabla \cdot [(\mu + \mu_T / \sigma_\varepsilon)\nabla \varepsilon] + C_{\varepsilon 1}(\varepsilon/k)(P+G) - C_{\varepsilon 2}\rho\varepsilon^2/k \quad (7)$$

where $P = \mu_T [\nabla \mathbf{u} : (\nabla \mathbf{u} + \nabla \mathbf{u}^T)]$ is the shear production and $G = (\mu_T / \mathrm{Pr}_T)\beta\mathbf{g} \cdot \nabla T$ accounts for the effect of the buoyancy on the production of turbulence.

Logarithmic form of turbulence equations

The turbulence equations (6), (7) are notoriously difficult to solve numerically. The eddy viscosity and several source terms contain division by the value of one turbulence variable. Negative or small values of the denominator can lead to improper sign or overly large values for μ_T or the source terms. This will cause a dramatic breakdown of the solution algorithm. Enhanced robustness of the algorithm will be achieved if one can ensure that turbulence variables remain positive throughout the domain and during the course of iterations. One way to preserve positivity of the turbulence variables consists in solving for their logarithms (Ilinca and Pelletier, 1998):

$$K = \ln(k), \qquad E = \ln(\varepsilon) \quad (8)$$

Solving for K and E guarantees that k and ε will remain positive throughout the computations. Hence the eddy viscosity μ_T will always remain positive. Moreover, solutions from logarithms are more accurate because the fields of the logarithmic variables K and E present smoother variations than those of k and ε. The turbulence equations and the eddy viscosity definition for logarithmic variables are as follows:

$$\rho\left(\frac{\partial K}{\partial t} + \mathbf{u} \cdot \nabla K\right) = \nabla \cdot \left[\left(\mu + \frac{\mu_T}{\sigma_k}\right)\nabla K\right] + \left(\mu + \frac{\mu_T}{\sigma_k}\right)(\nabla K)^2 + e^{-K}(P+G) - \rho e^{E-K} \quad (9)$$

$$\rho\left(\frac{\partial E}{\partial t} + \mathbf{u} \cdot \nabla E\right) = \nabla \cdot \left[\left(\mu + \frac{\mu_T}{\sigma_k}\right)\nabla E\right] + \left(\mu + \frac{\mu_T}{\sigma_k}\right)(\nabla E)^2 + C_{\varepsilon 1}e^{-K}(P+G) - \rho C_{\varepsilon 2}e^{E-K} \quad (10)$$

$$\mu_T = \rho C_\mu e^{2K-E} \quad (11)$$

Equations for logarithmic variables are equivalent to the original equations of the turbulence models. There is no change in the turbulence models and the only modification is that the computational variables are now the logarithms of the turbulence quantities.

3

Boundary conditions

Boundary conditions are specified on the strip and the inlet section (inductor inlet) as well as on the solid boundaries (walls) and on the top surface of the bath. The inductor inlet has been modeled using the specified flow rate and temperature increase. Velocity wall functions were used to model all solid surfaces including the pot walls, the moving strip and the rotating sink and stabilizer rolls. Heat transfer through all surfaces was modeled using convection boundary conditions and a temperature wall function.

Finite element solution

The global system of equations is solved in a partly segregated manner (Ilinca, Hétu and Ajersch, 2003). The solution algorithm is illustrated in Figure 2. At each time step global iterations are performed for the momentum-continuity, turbulence and energy equations. Sub-iterations of turbulence transport equations are also used to accelerate the overall convergence of the iterative process (Ilinca and Hétu, 2000). The transient solution is obtained during a time frame that covers several cycles of operation considering the initial temperature constant within the bath.

(I) - Time stepping iterations
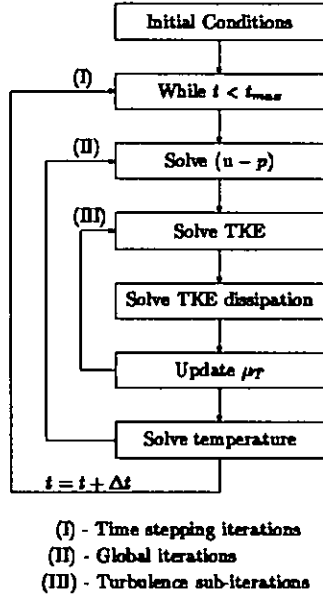(II) - Global iterations
(III) - Turbulence sub-iterations

Figure 2: Solution algorithm

The Navier-Stokes and scalar transport equations are solved using a Streamline-Upwind Petrov-Galerkin (SUPG) method (Franca and Frey, 1992). This method contains additional stabilization terms providing smooth solutions to convection dominating flows. The SUPG method also deals with velocity-pressure coupling so that equal-order interpolation results in a stable numerical scheme. This allows the use of simple linear elements for all variables.

Particle tracking algorithm

The propensity for bottom dross formation was measured by studying the movement of particles of different sizes in the bath. The particles are considered of spherical shape and submitted to the inertia, gravity, buoyancy and drag

forces. The momentum equation for a particle of diameter d is as follows:

$$M_p \frac{dv_p}{dt} = \left(\rho_p - \rho_l\right)\frac{1}{6}\pi d^3 g - 3\pi\mu d\left(v_p - v_l\right) \quad (12)$$

where M_p is the mass of the particle, v_p is the particle speed, v_l is the velocity of the melt, ρ_p and ρ_l are the densities of the particle and of the liquid melt respectively. The ratio between the density of the precipitated particles and the density of the melt affects the movement of particles through the buoyancy forces, whereas the particle size affects the buoyancy and drag forces.

The position of the particle as a function of time is determined by integrating the cinematic equation of motion:

$$\frac{dx_p}{dt} = v_p \quad (13)$$

The particle tracking is therefore performed by solving six equations, for the x, y and z components of the position and velocity:

$$\frac{dx_p}{dt} = u_p \quad (14)$$

$$\frac{dy_p}{dt} = v_p \quad (15)$$

$$\frac{dz_p}{dt} = w_p \quad (16)$$

$$M_p \frac{du_p}{dt} = -3\pi\mu d\left(u_p - u_l\right) \quad (17)$$

$$M_p \frac{dv_p}{dt} = \left(\rho_p - \rho_l\right)\frac{1}{6}\pi d^3 g_y - 3\pi\mu d\left(v_p - v_l\right) \quad (18)$$

$$M_p \frac{dw_p}{dt} = -3\pi\mu d\left(w_p - w_l\right) \quad (19)$$

This system of ordinary differential equations is solved by a highly accurate fourth order Runge-Kutta method (Press et al, 1992). The accuracy of the time integration procedure is therefore of Δt^5 where Δt is the time increment. The time increment was adapted to the size of the forces acting upon each particle such as the method performance to be optimal. As an example, for small particles the dominant force is the drag. In such a case the ratio of the drag force to the particle mass is proportional to the inverse of the square of the particle diameter. For accurate solutions the time increment must therefore also be kept as a proportion of the square of the particle diameter.

Special treatment is provided when particles travel from one element of the mesh to another. Because the velocity is linear inside elements, the method is highly accurate if each time step integration is made only inside a given element. Therefore, when reaching the interface between elements, the integration is made inside the current element up to the interface and then a new time integration step is performed in the second element.

VALIDATION OF THE MODEL

Validation of the CFD model predictions requires the measurement of fluid flow and temperature distribution in the melt. In the case of fluid flow, this has not been

4

attempted due to significant experimental difficulties. One example of flow measurements in a galvanized pot was presented by Toussaint et al, 1996. The measurements used a "floating ball device" and found an average circulation speed of 100 mm/s for a line speed of 140 m/min in one of Cockerill-Sambre's galvanizing pots at Ivoz-Ramet in Belgium (pot temperature 466°C and strip width 1100 mm). The authors stated that the fluid velocity and the pattern of the flow were in good agreement with the galvanizing model of Gagné, Paré and Ajersch, 1992. This early work used 3D water models and 2D CFD models. The more recent 3D CFD modeling indicates typical flow velocity of around 40 mm/s in a galvanizing bath with a strip speed of 105 m/min (Ajersch et al, 2001) although this is not the same bath as the earlier work. Another approach to validating the fluid flow predictions of the model is to compare CFD predictions and direct measurements of a water model. Recent water modeling has demonstrated good agreement with the CFD modeling approach developed at NRC (Ouellet, Ajersch and Ilinca, 2004) and used for this work.

Measurement of temperature is somewhat easier than fluid flow measurement but great care must be taken with calibration of the temperature measurement device. Such a measurement has been carried out on MCL1 over a period of 5 days using 3 Resistance Temperature Devices (RTD) located on the sink roll arm (Arm), on the sink-roll scraper blade (Blade) and near the control thermocouple (Pot). The results are in quite good agreement with the predictions of the CFD model. The temperature at the 5 locations is shown in Figure 3.

The following observations can be made (comparisons with the measured temperatures are given in italics):
- The temperature at all five locations shows a cyclic variation corresponding to the 12.2 minute cycle of the inductors. *This agrees with cyclic variation of the measured temperatures.*
- The amplitude of the temperature cycling varies from 2°C for the Blade RTD to 2.4°C for the Arm RTD. *The measured values have a lower amplitude of 1-1.5°C which could be explained by thermal lag due to the insulating effect of the sheaths on the thermocouples and RTDs.*
- The lowest temperature is shown by the Blade RTD. *This agrees with the measured values.*
- The temperature shown by the Arm and Pot RTDs are within 0.6°C of each other. *This agrees with the measured values.*
- The temperature at the location of T/C A and T/C B are within 0.2°C of each other and are 1°C above the temperatures of the Arm and Pot. *This agrees with the measured values. It is believed that the pot thermocouples record 5°C and 2.5°C higher values respectively.*
- The temperature at the five locations follows the sequence: Blade < Pot ≈ Arm < T/C B ≈ T/C A. *The measured values for the RTDs follow a comparable sequence Blade < Arm ≈ Pot < T/C B < T/C A.*

The above considerations give reasonable confidence that the model is correctly capturing the essential features of the ZINCALUME pot and gives reliable predictions.
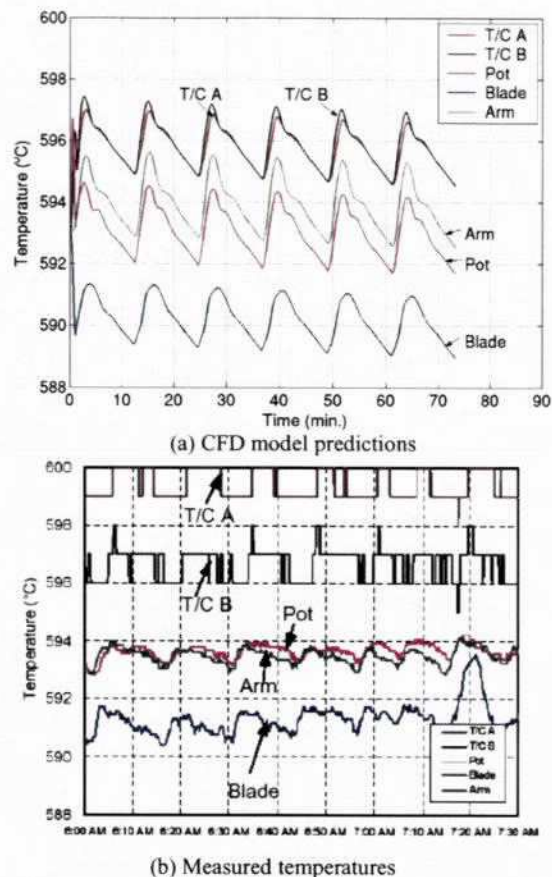

(a) CFD model predictions

(b) Measured temperatures

Figure 3: Predicted (a) and measured (b) temperatures at various locations inside the MCL1 pot

RESULTS

Selected results of the CFD model for MCL4 and MCL1 are illustrated for the condition at higher power setting 4B and 1C. These are presented in a series of comparisons in Figures 4 to 9 using two-dimensional sections through the pot for velocity distributions and three-dimensional portrayals for regions of low and high velocity. In the two-dimensional sections flow is portrayed using the particle traces that represent the flow over a period of 7.5 s. At the centre plane (Figure 4) the flow is restricted to the plane of the section (symmetry plane) but in the other sections there is usually a component of the flow out of the plane of the section (see Figures 8-9).

Flow Velocity

Fluid flow in the center plane of the bath is shown in Figure 4 and in a section through the inductor outlets in Figure 5. According to the model, for the cases studied, the fluid flow velocity in the melt has a maximum of around 500 mm/s in the vicinity of the moving strip surface and in the outlets and inlets to the inductors.

The flow through the inductors must satisfy the boundary conditions for mass flow rate for the cases studied: this varied from 79 to 125 tonnes/h for the MCL1 jet flow inductors and 22 to 45 tonnes/h for the MCL4 conventional inductors. Taking into account the different cross sectional areas of the two types of inductors this corresponds to flow rates at the inductor inlets of 720 to

5

1140 mm/s for MCL1 and 240 to 500 mm/s for MCL4. However, the model shows that for most of the pot volume the flow velocity is less than 50 mm/s (Figure 6). For Case 4B, for instance, 56% of the bath volume has a velocity of less than 30 mm/s. This can be compared to the line speeds, which ranged from 1583 mm/s (95 m/min) to 2833 mm/s (170 m/min). The melt velocity of most of the bath is therefore only 1% to 2% of the strip velocity. As expected, there are high velocity regions in the vicinity of the moving strip, the moving sink roll and stabilizer-roll surfaces as well as in the inductor inlets and outlets.

(a)   MCL4 (Case 4B)

(b) MCL1 (Case 1C)

Velocity (mm/s)
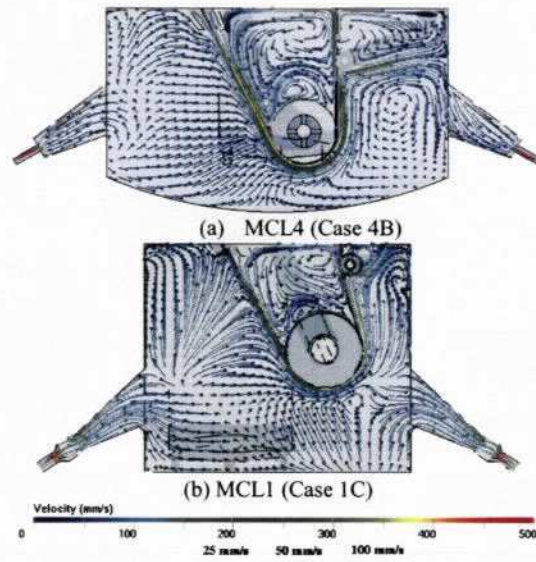
Figure 4: Flow at Z=0, centre line of pot

(a)   MCL4 (Case 4B)
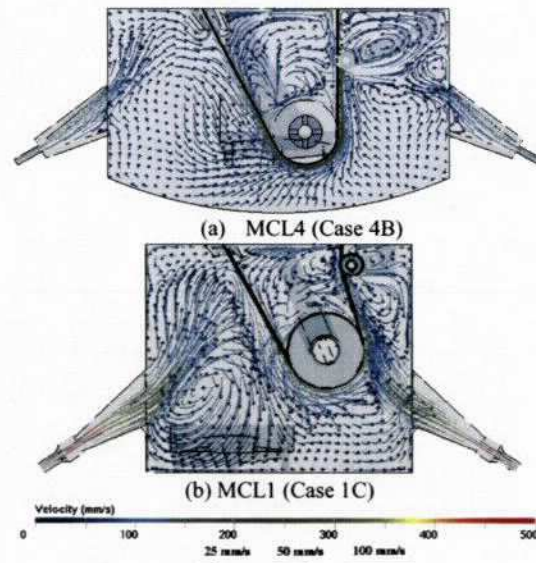

(b) MCL1 (Case 1C)

Velocity (mm/s)

Figure 5: Flow at Z=520, in-line with inductor outlets

Flow Direction

The flow in the bath is complex and three-dimensional. Specific differences in flow for the two different pots can be observed in Figures 4-9. The following general flow pattern trends are observed:

(a) Below the strip: There is a layer of rapid flow, about 100 mm thick, on either side of the strip surface. On the underside of the strip, flow moves with the strip, from strip entry in the snout, down to the sink roll and up to the stabilizer roll. For MCL4 the upward flow is diverted at the stabilizer roll nip and moves forward towards the front wall of the bath; this effect is less evident for MCL1 due to the different position of the stabilizer roll. At the entry end of the pot the flow is fed by molten metal coming from the bottom and sides of the pot and from the entry end inductor outlets. At the exit end of the pot the flow continues into the front inductor throat and feeds the flow into the centre channel of the exit inductor.

(b) Above the sink roll: A layer of rapid flow descends with the strip. This is fed by a flow near the surface of the melt flowing back from the strip exit towards the snout. At the sink-roll nip point the flow is ejected due to the movement of the top surface of the sink-roll, the resulting jet of fluid extending upwards towards the melt surface (Figures 4 and 6). At the outer edges of the strip the convergent flow also forms a lateral jet away from the nip point extending down towards the hearth of the pot, forming two recirculating zones (Figures 8 and 9).

(c) Above the stabilizer roll: At the strip centerline a layer of rapid flow ascends with the strip and is diverted along the surface towards the exit end of the pot. Some of the flow diverted by the stabilizer roll ascends up to the exit end of the pot. For MCL4 these flows create a separate, triangular region of melt, influenced by cooling from the air knives (Figures 10 and 11).
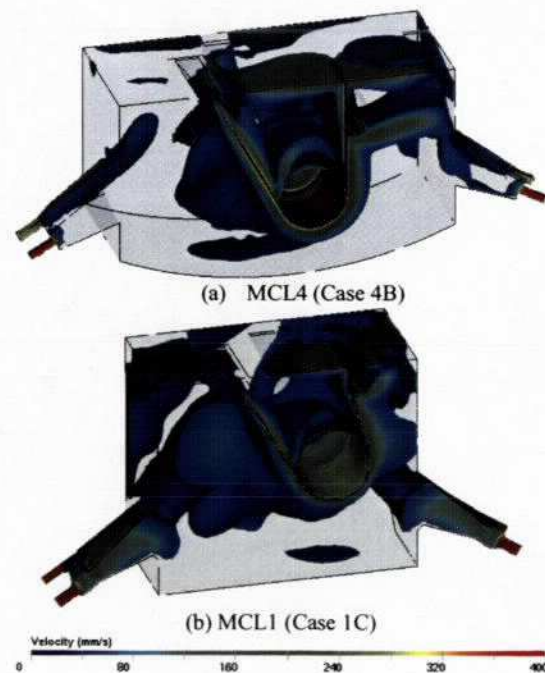

(a)   MCL4 (Case 4B)

(b) MCL1 (Case 1C)

Velocity (mm/s)

Figure 6: Regions with flow greater than 50 mm/s

(a) MCL4 (Case 4B)

(b) MCL1 (Case 1C)

Velocity (mm/s)
0   12   24   36   48   60
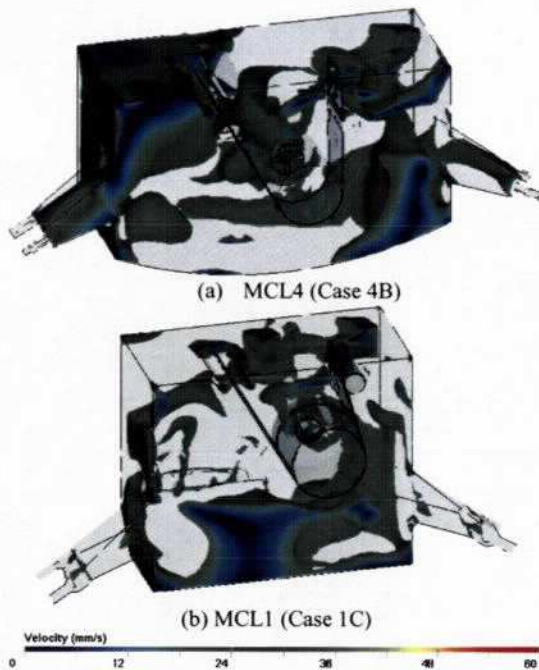
Figure 7: Regions with flow less than 20 mm/s

(d) The sides of the pot: In the lower regions of the pot, the flow rises from the bottom. In the upper regions the flow returns from the exit end of the pot to the entry end along the pot sidewalls. This return flow is perturbed by the flow associated with the side inductors, the strip exit, the sink-roll ends and the flow sideways from the nip point between the strip and the sink-roll.

(e) The bottom of the pot: The flow moving downwards with the strip moves forward and to the side along the hearth of the pot to form two recirculation zones towards the exit corners of the pot.

(f) In the inductor throats: Two recirculation zones exist between the inductor outlets and inlets. Thus, much of the flow that enters the inductor throat returns with the flow from the inductor outlets without passing through the inductor channels.
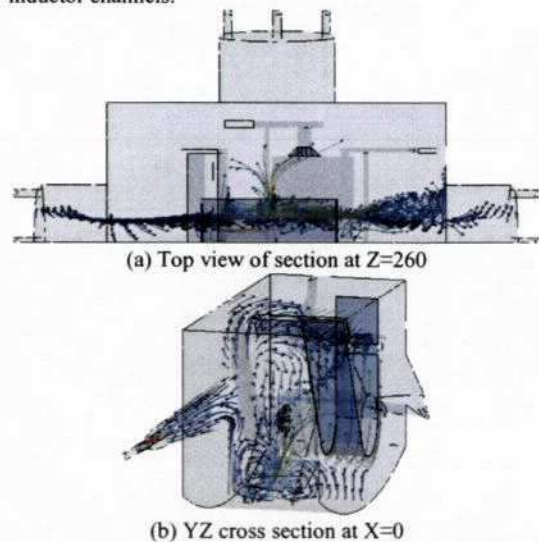

(a) Top view of section at Z=260

(b) YZ cross section at X=0

Figure 8: Flow at sink-roll nip point in MCL4

(a) Top view of section at Z=260
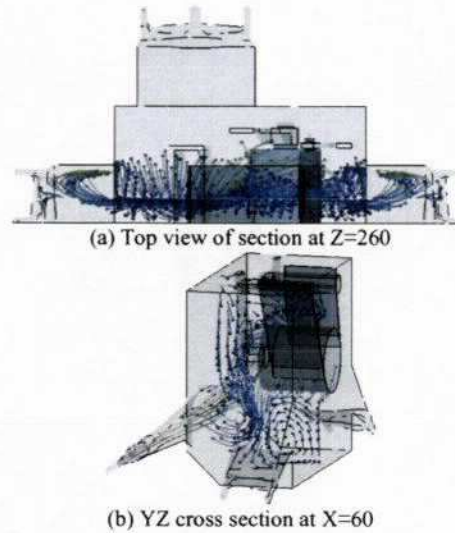

(b) YZ cross section at X=60

Figure 9: Flow at sink-roll nip point in MCL1

Temperature Distribution

As expected, the model indicates regions of low temperature surrounding the strip at strip entry (due to the cooling effect of the strip), at the bottom of the bath (due to the buoyancy) and at the surface of the melt near the strip exit (due to the cooling effect of the air knives) as shown in Figures 10-11. Also, as expected, the model indicates regions of high temperature emerging from the inductors and protruding into the bath. The most significant feature of the model is that it can predict a more detailed temperature distribution in the melt, as illustrated in the Figures 10-11.
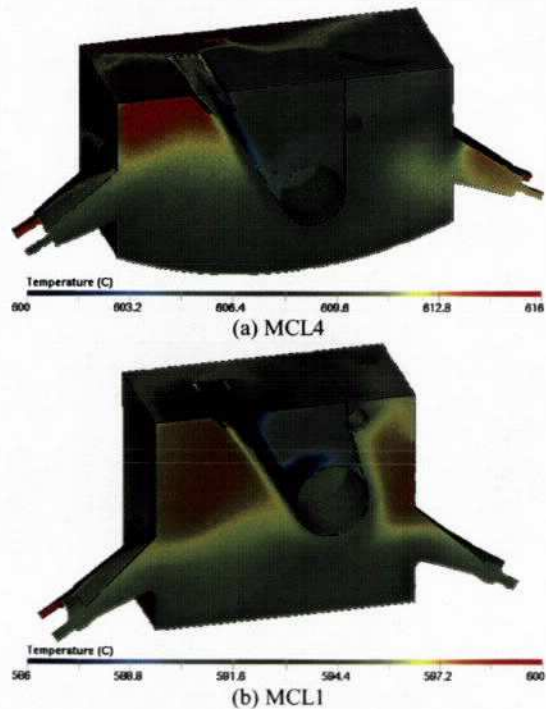

Temperature (C)
600   603.2   606.4   609.6   612.8   616
(a) MCL4

Temperature (C)
586   588.8   591.6   594.4   597.2   600
(b) MCL1

Figure 10: Temperature distributions

7

(a) T<609C in MCL4
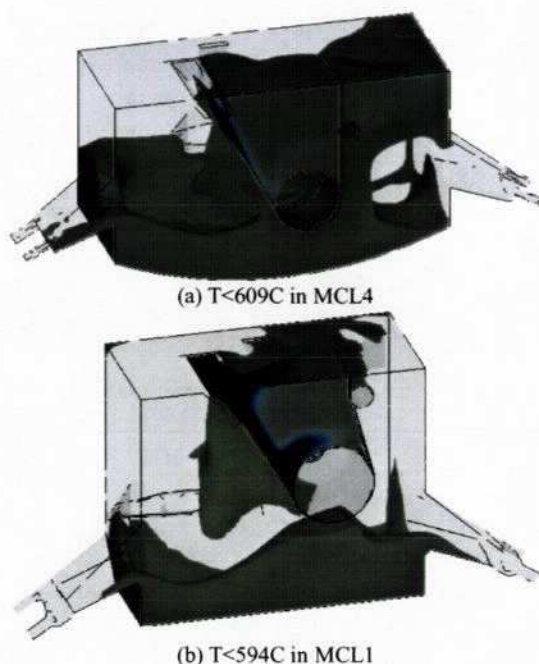

(b) T<594C in MCL1

Figure 11: Regions with low melt temperature

For MCL4, the average bath temperature is 608°C but there are substantial volumes of the melt that are 2-8°C cooler or 4-8°C hotter. At very localized regions near the exit from the inductors the melt will be 21°C hotter according to the imposed operating conditions for the conventional Ajax inductors. For MCL4 a cold region of the bath was found at the centre of the exit end, extending diagonally down to the stabilizer roll caused by the recirculating flow in this region. The surface of the melt between the snout and the strip exit is also cooled by the air knives and a cool region extends into the v-shaped region above the sink-roll. The jet of cooler melt that originates in the nip where the strip meets the sink-roll also influences this region. A jet of cooled melt also extends sideways and to the bottom of the pot from the side of the sink roll at the nip where the strip meets sink-roll (Figure 9). The melt is also cooler at the bottom of the pot, particularly at the pot corners. With the inductors operating on an intermediate power setting of 235 kW, hot regions of the melt were observed at the entry end, behind the snout and also at either side of the snout. This is caused by hot metal flowing upwards from the entry end and side inductor outlets into a region of the melt that is not cooled by the air knives and which has relatively low fluid flow velocity (Figure 7). At the exit end of the pot, the inductor outlet flow is prevented from rising to the pot surface by the flow imposed by the strip movement. MCL1 shows less temperature variation overall due to the greater stirring arising from the use of jet flow inductors (higher flow rate and smaller temperature increase). The higher flow rate combined with the smaller pot volume and the lower position of the inductors on the side-wall also enables more direct interaction between the hot melt from the inductors and the cooled melt associated with the boundary layer moving with the strip (compare Figures 5a and 5b).

MCL1 and MCL4 compared

Significant differences between the flow were observed when comparing MCL4 and MCL1, which may be associated with bottom dross formation in MCL4 and may explain its absence in MCL1:

- The flow from the inductors in MCL1 causes much more stirring in the melt when compared to MCL4. This is due to a combination of the smaller pot size, the different location of the inductors throats relative to the sink roll and the use of jet flow inductors on MCL1. The flow from the inductors in MCL1 interacts more directly with the strip than it does in MCL4.
- The recirculating region above the stabilizer roll in MCL4 is almost absent in MCL1 due to the higher location of the stabilizer roll and the proximity of the exit wall of the pot.
- The jet of cooled melt that flows sideways from the nip point between the strip and the sink roll is directed to the bottom of the pot as two recirculating zones in MCL4. This is less well established in MCL1.
- The volume fraction (and total volume) of the pot affected by low velocity is greater in MCL4 than in MCL1. This is quantified in Figure 12.
- The temperature distribution in MCL1 is more uniform than that in MCL4. In particular MCL4 has a hot zone behind the snout that is largely absent in MCL1.
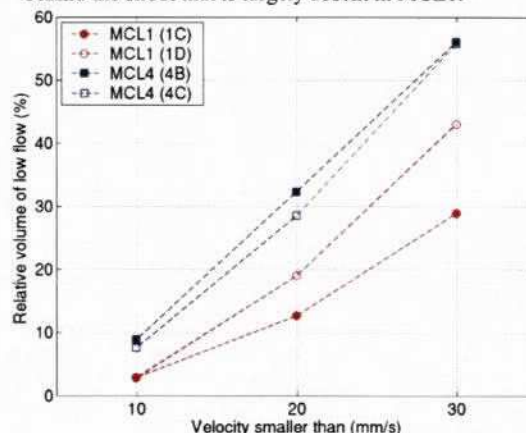

Figure 12: Relative volume of low flow for MCL1 and MCL4

The above observations support the hypothesis that the bottom dross formation in MCL4 is caused by the settling of particles of suspended dross in regions of low flow velocity in the melt.

Propensity for bottom dross formation

The propensity for bottom dross formation was measured by following in time the spatial distribution of a large number of particles (8000 for each particle size), which are initially uniformly distributed within the bath volume. Particle tracking was carried out separately for five different sizes of particles (100μm, 50μm, 20μm, 10μm, and 5μm) and for a period of time equal to the inductor cycling time. The particle density was taken to be twice that of the fluid.

For the initial uniform distribution 22% of particles for MCL1 and 17% for MCL4 are located within the bottom region. Figure 13 illustrates the relative change in the number of particles at the bottom of the bath after one

complete cycle as a function of the particle size. The bottom region is considered as having the height equal to a fifth of the pot height. The results for the operation using jet-flow inductors for both MCL1 and MCL4 pots are compared. We can see that the number of particles settling at the bottom after one cycle increases with the particle size. In the case of large particles, the proportion of particles settling at the bottom of the bath is higher in the case of the MCL4 pot. For particles with a diameter of 100 μm, 70% are found at the bottom of the bath after one cycle for MCL4 (an increase of 310% over the initial distribution), whereas 60% goes to the bottom for the MCL1 pot (an increase of 170% over the initial distribution). This agrees well with the observed build-up of bottom dross in the MCL4 pot.
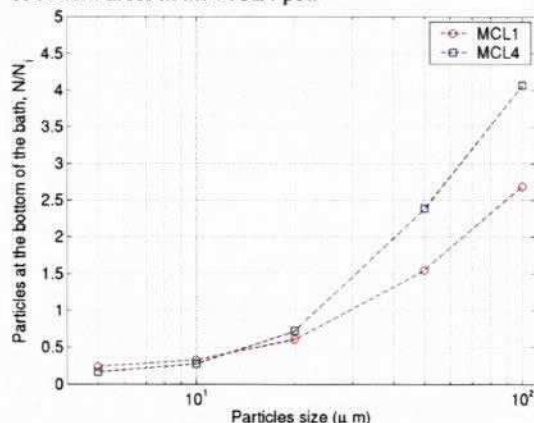

Figure 13: Particles at the bottom of the pot after 1 cycle

CONCLUSION

CFD modeling has been used to calculate the fluid flow and temperature distribution within the ZINCALUME coating pots at MCL4, Western Port, and MCL1, Port Kembla. Results indicate that the MCL1 pot has a more uniform temperature distribution and greater amount of stirring than MCL4. Also, flow from the inductors impinges more directly on the strip for MCL1 than for MCL4. MCL4 has a higher volume fraction of the melt affected by low flow regions, an observation that is consistent with the hypothesis that the increased rate of bottom dross formation for MCL4 compared to MCL1 is due to a generally lower velocity regime promoting the settling of suspended intermetallic particles. Particle tracking indicates that large particles are more prone to settle at the bottom of the bath for the MCL4 when compared with MCL1.

ACKNOWLEDGMENTS

REFERENCES

WILLIS, D.J. and SETARGEW, N., (2002), "Bottom dross formation mechanisms in ZINCALUME coating line pots", *InterZAC 2002*.

SETARGEW, N. and WILLIS D.J., (2003), "Detection of dross intermetallic particles in ZINCALUME melt using LAIS," *PacZAC2003*.

WILLIS, D.J., ILINCA, F. and AJERSCH, F., (2004), "Fluid flow modelling in a 55%Al-Zn pot", *Galvatech 2004*, 905-916.

GAGNÉ, M., PARÉ, A. and AJERSCH, F., (1992), "Water modeling of a continuous galvanizing bath", *The 84th Galvanizers Assoc.*, Pittsburgh, PA, 142-163.

TOUSSAINT, P., VERNIN, P., SYMOENS, B., SEGERS, L., TOLLEY, M., WINAND, R. and DUBOIS, M., (1996), "Experimental determination of velocity flow fields in continuous hot dip galvanizing baths", *Ironmaking & Steelmaking*, **23** (4), 357.

GAGNÉ, M. and AJERSCH, F., (1995), "Galvanizing bath water model tests by monitoring pH changes from localized acid additions", *Galvatech'95*, 687.

PARÉ, A., BINET, C. and AJERSCH, F., (1995), "Numerical simulation of 3-D flow in continuous strip galvanizing bath", *Galvatech'95*, 695-706.

GAGNÉ, M. and GANG, M., (1998), "Numerical modeling of fluid flow pattern in a continuous galvanizing bath," *Galvatech'98*, 90-95.

OTSUKA, K., ARAI, M. and KASAI, S., (1998), "Development of dross control methods in a continuous galvanizing pot by numerical bath flow analysis," *Galvatech'98*, 96-101.

EVANS, K.J. and TREADGOLD, C.J., (1999), "Modelling and measurement of transient conditions in the galvanizing pot", *Galvanizers Assoc.*, Jackson, MS, 131.

AJERSCH, F., ILINCA, F., PERRAULT, M., MALO, A. and HÉTU, J.-F., (2001), "Numerical analysis of the effects of operating parameters on flow in a continuous galvanizing bath," *Galvatech'2001*, 511.

KOBAYASHI, E., MARUYAMA, M., UNEDA, H., (1996), "Entrapment of Suspended Dross Particles in the Coreless Pot during Galvalume Production", *InterZAC 1996*.

LAUNDER, B.E. and SPALDING, D.B., (1972), *Mathematical Models of Turbulence, 6th ed.*, Academic Press, London.

ILINCA, F., HÉTU, J.-F. and AJERSCH, F., (2003), "Three-dimensional Numerical Simulation of Turbulent Flow and Heat Transfer in a Continuous Galvanizing Bath," *Num. Heat Transfer, Part A: Appl.*, **44**, 463-482.

ILINCA, F. and HÉTU, J.-F., (2000), "Finite Element Solution of Three-Dimensional Turbulent Flows Applied to Mold-Filling Problems," *Int. J. for Numerical Methods in Fluids*, **34**, 729-750.

FRANCA, L.P. and FREY, S.L., (1992), "Stabilized Finite Element Methods: II. The incompressible Navier-Stokes equations," *Computer Methods in Applied Mechanics and Engineering*, **99**, 209-233.

ILINCA, F. and PELLETIER, D., (1998), "Positivity Preservation and Adaptive Solution of the k-ε Model of Turbulence," *AIAA Journal*, **36**(1), 44-50.

PRESS, W.H., FLANNERY, B.P., TEUKOLSKY, S.A., and VETTERLING, W.T., (1992), "Numerical Recipes in FORTRAN: The Art of Scientific Computing", 2nd ed., Cambridge University Press, 704-716.

OUELLET, L., AJERSCH, F. and ILINCA, F., (2004), "Numerical Simulation and Validation of Flow in a Galvanizing Bath Using a Water Model", *Galvatech2004*, 917-926.